Journal of Materials Chemistry A

PAPER

Low temperature grown $CuBi_2O_4$ flower morphology and its composite with CuO nanosheets for photoelectrochemical water splitting†

Cite this: DOI: 10.1039/c3ta14906d

Rupali Patil,[ab] Sarika Kelkar,[ab] Rounak Naphade[ab] and Satishchandra Ogale*[ab]

Received 26th November 2013
Accepted 23rd December 2013

DOI: 10.1039/c3ta14906d

www.rsc.org/MaterialsA

In this work we highlight a peculiar synthesis protocol for the p-type ternary metal oxide system of copper bismuth oxide ($CuBi_2O_4$), which yields a highly crystalline spherulitic morphology at a low temperature of 78 °C. We associate this growth with the hydrogen bonding effects imparted by the ethanol–water co-solvent system used for the synthesis. We present a detailed growth mechanism by evaluating different synthesis conditions systematically. Furthermore we show that upon the use of the non-stoichiometric (excess copper) precursor mixture under the same experimental conditions the growth of spherulitic $CuBi_2O_4$ changes the size and type of the spherulites. Interestingly, careful optimization of the non-stoichiometric synthesis presents a complete impediment to the spherulitic growth and produces a composite of nanorods of $CuBi_2O_4$ and nanosheets of CuO. This anisotropic nanocomposite shows an order of magnitude higher surface area as compared to spherulitic $CuBi_2O_4$. Since both $CuBi_2O_4$ and CuO are visible light absorbing p-type semiconductors, when the synthesized nanocomposite materials are examined as photoelectrochemical (PEC) photocathodes for water splitting, they show a remarkable dependence on the morphology and phase constitution. Almost 13-fold stronger PEC response is observed as the morphology changes from spherulites to nanorods.

Introduction

Controlled synthesis of anisotropic, well-aligned semiconductor nanostructures has attracted increasing attention because of their superior electronic and surface properties. These properties are most important for photoelectrochemical (PEC) applications where the maximum electrode–electrolyte interface area and efficient charge transport are desired. In this regard, many metal oxides (being the most explored systems for PEC applications due to their stability) have been synthesized and studied with different anisotropic morphologies such as nanorods, nanotubes, nanowires, *etc.*[1–5] Many physical and chemical synthesis methods such as chemical vapour deposition, solution growth methods and hydrothermal methods have been employed in this regard to obtain different morphologies.[6–8] So far most of the explored systems have been primarily binary metal oxides such as TiO_2, ZnO, Fe_2O_3, Cu_2O, *etc.* where formation of the desired pure phase is more straightforward[9–11] and/or which have the crystal structure having tendency to grow favourably along one particular crystal plane. In contrast, in the case of multi-component oxide systems, things become more complicated, since a minute synthetic perturbation can drive the reaction towards formation of binary impurity phases in coexistence with the desired pure ternary phase. Therefore, while many multi-component metal oxide systems are worthy of explorations for optoelectronic and PEC applications, very few have been investigated thus far with optimum control over morphology and phase constitution. We have been studying some n and p type multinary metal oxide systems in the context of the PEC application. We have found that the n-type cadmium tin oxide system (Cd_2SnO_4) shows a fairly good photoanode performance,[12] and upon further careful engineering of the system a remarkable (over 40 fold) enhancement in the PEC performance can be realized.[13] This has encouraged us to study other favourable multinary metal oxide systems in depth and engineer their constitution and properties towards the PEC application. While we focus on the PEC application, it is clear that these nanostructures could be interesting to other opto-electronic applications as well. In the present report we have selected an interesting p-type ternary metal oxide system: Copper Bismuth Oxide ($CuBi_2O_4$).

With a band gap of 1.7 eV, $CuBi_2O_4$ is clearly a useful material for optical applications. Unfortunately its electronic properties such as conductivity and mobility are not very

[a]Centre of Excellence in Solar Energy, Physical and Materials Chemistry Division, National Chemical Laboratory (CSIR-NCL), Pune 411 008, India

[b]Network Institute of Solar Energy (CSIR-NISE), New Delhi, India. E-mail: sb.ogale@ncl.res.in

† Electronic supplementary information (ESI) available. See DOI: 10.1039/c3ta14906d

favourable for certain applications.[14] This requires further research on this material with regard to doping, microstructure/morphology control (finer scale nano-structuring leading to the minimal carrier transport distance to the surface), and hetero-structuring which can possibly improve the charge separation properties. So far the synthesis protocol strategies for obtaining copper bismuth oxide have been limited to solid state reaction,[14–16] electrodeposition[17] and the hydrothermal process,[18] all involving the use of stoichiometric proportions of Bi_2O_3 and CuO or their precursors and producing mostly spherical nanoparticulate morphology.[17,18] All of these methods require higher temperature/pressure or voltage to obtain pure phase $CuBi_2O_4$.

In the current work we explore an alternative synthesis protocol utilizing the mixture of ethanol and water as a co-solvent and take advantage of the hydrogen bonding effects to achieve preferential growth of certain planes as well as formation of clusters rendering spherulitic structures. Importantly, the entire synthesis process takes place without the use of any surfactant or template, at a low temperature of only 78 °C over a time duration of two hours. In order to understand the underlying mechanism of morphology evolution, we have varied the temperature, time and ethanol concentration systematically. The stoichiometric addition of copper and bismuth (0.5 : 1) precursors predominantly forms spherulitic flowers. Interestingly, upon addition of excess copper precursor (non-stoichiometric growth) the formation of spherulite is disturbed. In fact, beyond a specific level of excess Cu, no spherulites are formed, yielding a mixed phase of $CuBi_2O_4$ and CuO having anisotropic morphology of nanorods and nanosheets, respectively.

The schematic of formation of pure $CuBi_2O_4$ and non-stoichiometric $CuBi_2O_4$ is shown in Scheme 1. The $CuBi_2O_4$–CuO system shows an almost 10 times higher surface area than pure $CuBi_2O_4$. Hence we investigated these cases as photocathodes for PEC water splitting applications. We observed a remarkable (an almost 13-times) increase in the photocurrent. We present a detailed discussion on the morphology evolution and disruption, and correlate it with the PEC water splitting performance.

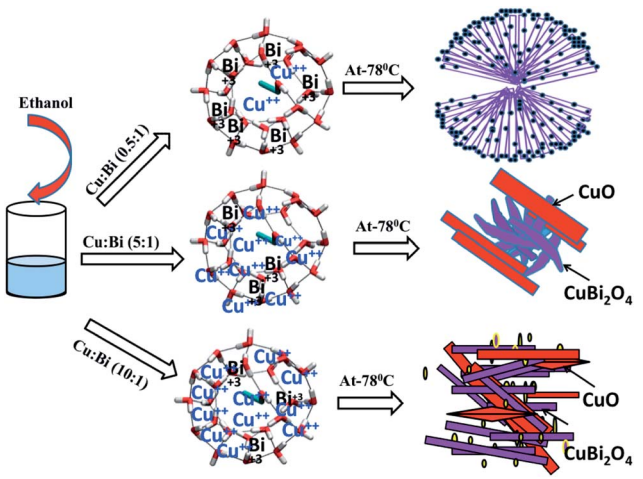

Scheme 1 Schematic of precursor ratio controlled morphology evolution.

Experimental details

Synthesis. For the synthesis of pure $CuBi_2O_4$, 1 mole of bismuth nitrate pentahydrate (Thomas Bakers) was dissolved in 60 mL deionised water with 2 mL nitric acid. The solution was stirred for two hours for complete dissolution of the bismuth precursor. Subsequently aqueous solution containing 0.5 mole of copper sulphate pentahydrate (Merck) was dissolved in 30 mL deionised water and added into the bismuth solution. Further ethanol was added to this reaction mixture (in varying quantity as discussed below) and the solution was slowly heated to 78 °C. Then 1 M NaOH solution was added for the precipitation of salt and the pH of the reaction reached 10. The reaction mixture turned dark blue. After two hours of stirring the reaction mixture changed its colour to dark brown (colour of pure $CuBi_2O_4$). The powders thus obtained were centrifuged, washed with DI water–ethanol and dried in an oven at 80 °C. For control, pure CuO was also prepared using the same protocol. For the understanding of the morphology evolution, the specific process parameters were systematically varied as presented below.

Type of solvent. The effect of solvent on the morphology was studied by synthesis of $CuBi_2O_4$ in water, ethanol and the mixture of water–ethanol.

Water–ethanol ratio. The effect of ethanol concentration was studied by varying the water to ethanol ratio as 4 : 1, 4 : 3, 2 : 1, and 1 : 1.

Temperature. The effect of temperature on the morphology of $CuBi_2O_4$ was studied by performing synthesis at 45 °C, 65 °C and 78 °C.

Process duration. Time dependent morphology evolution was studied over a period of two hours.

Non-stoichiometry. The effect of non-stoichiometry on the phase(s) and morphology was studied by the addition of excess copper to the reaction mixture in mole ratios of copper : bismuth of 5 : 1, 10 : 1, and 15 : 1. The 10 : 1 mole ratio sample showed the highest PEC performance (and is addressed as the $CuBi_2O_4$–CuO composite in the rest of the manuscript).

Characterization. The $CuBi_2O_4$ samples obtained at different temperatures were characterized by X-ray diffraction (XRD) and scanning electron microscopy (SEM). All the characterizations were performed on pure $CuBi_2O_4$, pure CuO and the optimized $CuBi_2O_4$–CuO composite for comparison and analysis. The crystal structure was analyzed using a Pan-analytical X-Ray diffractometer equipped with a quartz monochromator and Cu K_α radiation ($\lambda = 0.154$ nm). The UV-visible diffuse reflectance spectra were obtained using a Varian Cary model 5000 spectrophotometer. The microstructural analysis and elemental mapping were carried out by FE-SEM using an FEI QUANTA 200, and by HRTEM using an FEI Tecnai 300. The surface area measurements were performed using a Gemini Model 2390 device and calculated according to the Brunauer–Emmett–Teller (BET) equation.

Photoelectrochemical measurements. The photoelectrodes were prepared by a doctor-blading method on fluorine doped tin oxide (FTO) coated glass. Triton X-100 and polyethylene glycol additives were used for obtaining uniform, porous and

adhesive films. The films were heat-treated at 400 °C for 1 h to remove the additives.

A three electrode system was used with $CuBi_2O_4$, CuO or the $CuBi_2O_4$–CuO composite film forming the working electrode(s), Pt wire as the counter electrode and Ag/AgCl as the reference electrode. In all the PEC measurements 0.1 M sodium sulphate was used as the electrolyte. An Autolab PGSTAT 30-Eco-Chemie was used to sweep the voltage at a scanning rate of 10 mV s^{-1} and the current was measured in the chopped irradiation in the dark and under 1 sun (AM 1.5 conditions, Newport solar simulator). The stability was also studied under the same conditions by applying −0.4 V *vs.* Ag/AgCl.

Results and discussion

Effects of solvents

With the stoichiometric amounts of copper and bismuth precursors, the synthesis was carried out in water, ethanol and a mixture of water–ethanol. In the case of the water–ethanol mixture we also studied cases of different component ratios, the discussion of which is presented in the next section. However as a representative case here we present the case of the water to ethanol ratio of 1 : 1. Fig. 1(A)–(C) show the effects of solvents on the morphology of $CuBi_2O_4$ and Fig. 1(D) shows XRD patterns for these three cases. The XRD patterns for $CuBi_2O_4$ in water and the water–ethanol mixture show formation of pure phase tetragonal $CuBi_2O_4$ (PCPDF #48-1886). However, the XRD pattern of $CuBi_2O_4$ synthesized in pure ethanol shows the presence of some impurity phases from the precursor salts. This is due to the incomplete solubility of Bi and Cu precursors in ethanol. In the presence of water the precursors form a more homogeneous solution which facilitates pure phase formation.

In the case of water based synthesis 2 to 3 micron-sized spherical $CuBi_2O_4$ particles are obtained at 78 °C, after 2 h of reaction. This can be attributed to the formation of hydrogen bonded (adjacent H_2O molecules) clusters into which the precursor Cu and Bi cations could get trapped. In ethanol, however, there seems to be evolution of porous cube-like faceted morphology. Interestingly, when the water–ethanol mixture is used in the reaction, spherulitic morphology is obtained. More specifically these are two-eyed, type II spherulitic structures. We observed that upon addition of ethanol into the water-precursor mixture, there is a sudden increase in viscosity. This can be due to a couple of things; firstly upon ethanol addition, the already existing hydrogen bonded structures within water would get disturbed and there is rearrangement of –OH hydrogen bonds, forming bigger clusters (with the hydrophobic end of ethanol at the exterior side-like micelles), and secondly, this would increase the concentration of solvated precursors in water as compared to hydrogen bonded dimers/trimers. With the higher ratio of ethanol : water, the increase in saturation index of the precursors is higher. This drives the reaction into self-precipitation and now upon increase of temperature to 78 °C, when ethanol starts evaporating, spherulitic structures of $CuBi_2O_4$ are obtained.

Effects of ethanol concentrations

The data presented in Fig. 2 reveal the effects of ethanol concentrations on the spherulitic growth of $CuBi_2O_4$, by varying the water–ethanol ratio as 4 : 1 (A), 2 : 1 (B), 4 : 3 (C) and 1 : 1 (D). It is observed from Fig. 2(C) and (D) that beyond the water to ethanol ratio of 2 : 1, spherulitic morphology evolves. Below this ratio a more sphere-like morphology is observed. The higher concentration of ethanol reduces the solubility of Cu and Bi precursors in water and increases the concentration of solvated precursors relative to hydrogen bonded dimers/trimers, thus increasing the driving force towards precipitation and crystallization at low temperature.

Effects of temperatures

In order to further understand the morphology evolution in the case of the water–ethanol mixture, three samples synthesized at

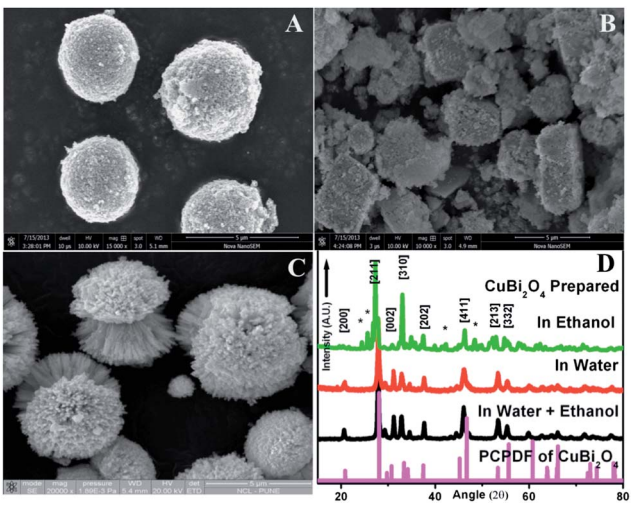

Fig. 1 SEM images of $CuBi_2O_4$ synthesized in water (A), ethanol (B) and in the water–ethanol mixture (C), XRD patterns of A, B and C (D) (* indicates the impurity peaks).

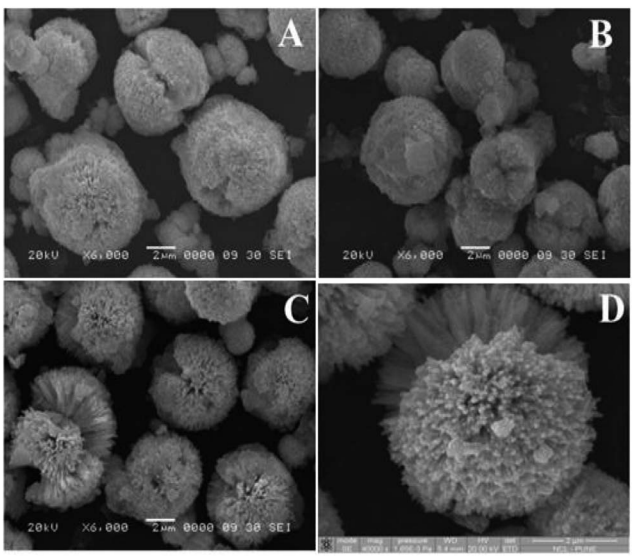

Fig. 2 Morphology change obtained by 78 °C by changing the water–ethanol ratio: 4 : 1 (A), 4 : 3 (B), 2 : 1 (C) and 1 : 1 (D).

45 °C, 65 °C and 78 °C were investigated. The corresponding SEM images and XRD data are shown in Fig. 3. In the 45 °C case the microstructure looks like interconnected nanoparticles of size 50 to 100 nm, which in the XRD data shows only a slight peak at 28.3° corresponding to the [211] peak for $CuBi_2O_4$. Interestingly by increasing the synthesis temperature by 20 °C *i.e.* at 65 °C a well crystalline tetragonal phase of $CuBi_2O_4$ is formed with a morphology of uniform porous spheres of size around 2–3 microns.

When the temperature was further increased to 78 °C, which is the same as the boiling point of ethanol, the porous spheres symmetrically break into spherulitic flowers assembled of nanorod-like structures.

Thus at such a low processing temperature due to the synergistic effect of hydrogen bonding and solvent evaporation, a highly crystalline and defined morphology of $CuBi_2O_4$ is formed by this method.

Effects of reaction times

In order to study the kinetics of morphology evolution more carefully (nucleation, crystal growth and Ostwald's ripening process), we monitored the case of 1 : 1 water–ethanol, processed at 78 °C at different time intervals up to two hours. Fig. 4 shows the SEM images of the samples collected at 0 min, 30 min, 60 min and 120 min. We collected the zero minute case when the reaction mixture had just reached 78 °C. It can be clearly seen from the SEM images that the morphology evolves from interconnected nanoparticles to sphere-like structures to two-eyed spherulites. During the first hour, the self-assembly of nanoparticles into spheres appears to be driven by the alkaline pH of the medium and densification (higher viscosity) as more and more ethanol gets evaporated from the system. The presence of OH– (from added NaOH) can influence the agglomeration of primary nanocrystals into larger clusters. According to a popular model[19,20] the formation of mesoscale assembly is based on self-organization of crystalline building blocks through the spontaneous coalescence of primary nanoparticles into colloidal aggregates. This way the adjacent nanoparticles are self-assembled by sharing common crystallographic orientation and by docking themselves at a planar interface.[21] The driving force for this spontaneous oriented attachment is the reduction in the surface free energy.[22] Additionally the hydrogen bonding encourages the molecules to self-assemble into larger aggregates. Such self-assembling conformations break after 90 minutes, leading to spherulitic flowers.

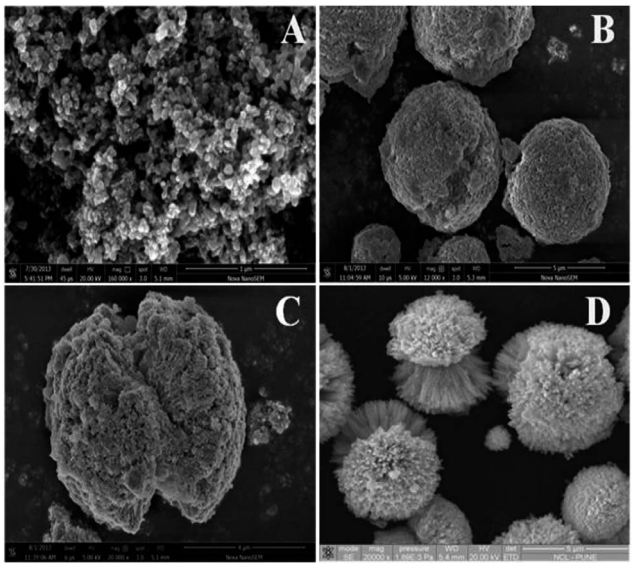

Fig. 4 SEM images of $CuBi_2O_4$ obtained at 0 min (A), 30 min (B), 60 min (C) and 120 min (D) respectively.

Effects of precursor stoichiometry

Fig. 5 shows HRTEM images of the $CuBi_2O_4$–CuO 10 : 1 Cu : Bi optimized case (A and B) and their respective lattice fringes (C and D).

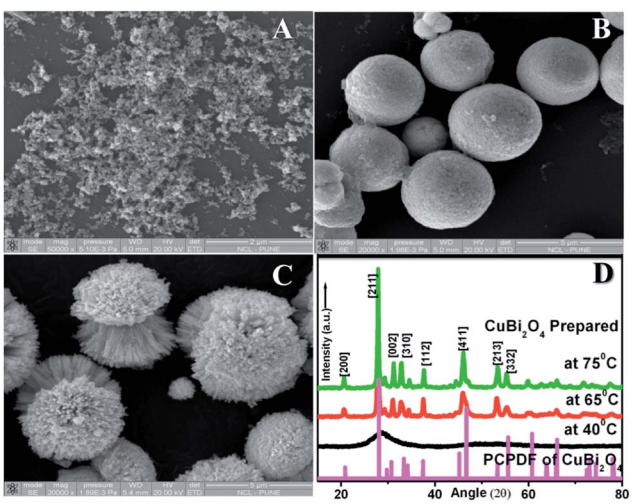

Fig. 3 SEM images of $CuBi_2O_4$ obtained at different temperatures from 45 °C (A), 65 °C (B), 78 °C (C), and corresponding XRD patterns (D).

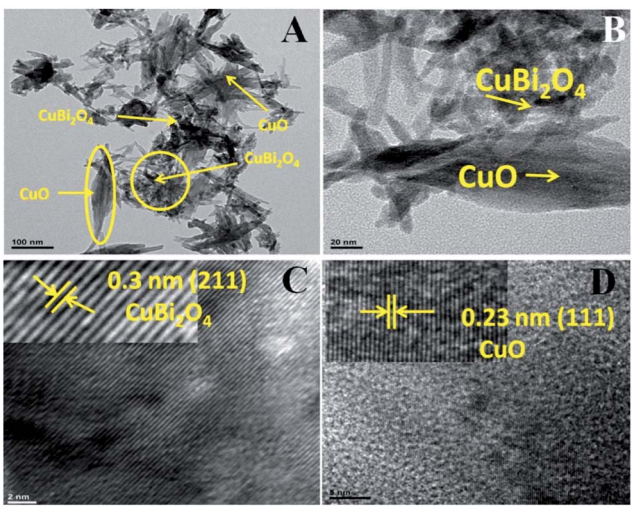

Fig. 5 HRTEM images of the $CuBi_2O_4$–CuO 10 : 1 Cu : Bi optimized case (A and B) and their respective lattice fringes (C and D).

The normal spherulitic growth of pure $CuBi_2O_4$ was obtained at 78 °C with the cationic ratio Cu : Bi of 0.5 : 1 and water- : ethanol ratio of 1 : 1 (as seen in Fig. 4D). Under these experimental conditions when excess of copper precursor was added, a composite of $CuBi_2O_4$ and CuO was obtained, and most interestingly a remarkably different morphology evolution was observed. Fig. 5 shows the HRTEM images of a representative case (Cu : Bi, 10 : 1) of the non-stoichiometrically prepared $CuBi_2O_4$–CuO composite. The TEM images of other non-stoichiometric cases of 5 : 1 and 15 : 1 are presented in ESI-I.† In all these cases a mixture of $CuBi_2O_4$ and CuO was observed (the latter formed from the excess of copper precursors added during synthesis). The two different phases of $CuBi_2O_4$ and CuO can be identified *via* their different (*Z*) contrasts and lattice constants as well. CuO gives a lower contrast as it forms thinner sheet-like structures, while $CuBi_2O_4$ appears darker and has high *Z* element Bi. This is confirmed by the independent TEM images of pure phased $CuBi_2O_4$ and CuO samples as shown in ESI-II.† Interestingly, as observed in Fig. 5(A) and (B) and ESI-I,† $CuBi_2O_4$ is observed to form smaller spherulitic structures as the excess-copper content is increased. For example the spherulites in pure $CuBi_2O_4$ (0.5 : 1 stoichiometry, Fig. 4D) are in the range of 2–3 microns, and those in the case of 5 : 1 non-stoichiometry (ESI-IA†) are of the size around 100–200 nm. A further increase in the nonstoichiometric ratio of cations Cu : Bi to 10 : 1 (Fig. 5A) and 15 : 1 (ESI-IB†) is seen to disrupt the spherulite formation strongly. As seen in Fig. 5B there are very few spherulites and they are less than 100 nm in size. The data on elemental mapping of the $CuBi_2O_4$–CuO composite are provided in Fig. 6. This elemental mapping further confirms the concurrent presence of $CuBi_2O_4$ and CuO in the nanocomposite.

We believe that due to the difference in the crystal structures of $CuBi_2O_4$ (tetragonal) and CuO (monoclinic), the presence of CuO disturbs the self-assembly of $CuBi_2O_4$ into spherulite configuration. Since CuO has a tendency to form nanosheets under this reaction environment, the final product is a mixture of CuO nanosheets and $CuBi_2O_4$ nanorods. The CuO nanosheets are around 200 nm in length and 20 nm in width, while $CuBi_2O_4$ nanorods have dimensions of 2 micrometer in length and 20 nm in width, as shown in individual TEM images of ESI-II.†

The X-ray diffraction patterns for the nonstoichiometric cases are shown in Fig. 7. They show formation of both tetragonal and monoclinic phases of $CuBi_2O_4$ (PCPDF #48-1886) and CuO (PCPDF #80-1917), respectively.

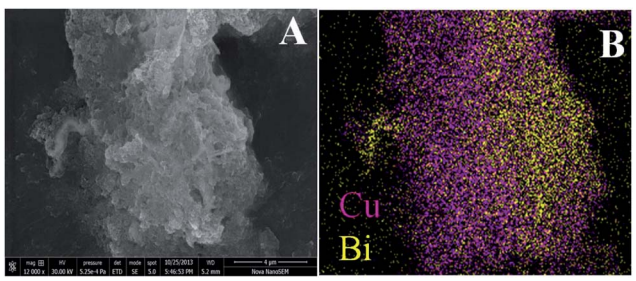

Fig. 6 FE-SEM image (A) and elemental mapping image (B) of the $CuBi_2O_4$–CuO composite obtained from energy dispersive X-ray analysis.

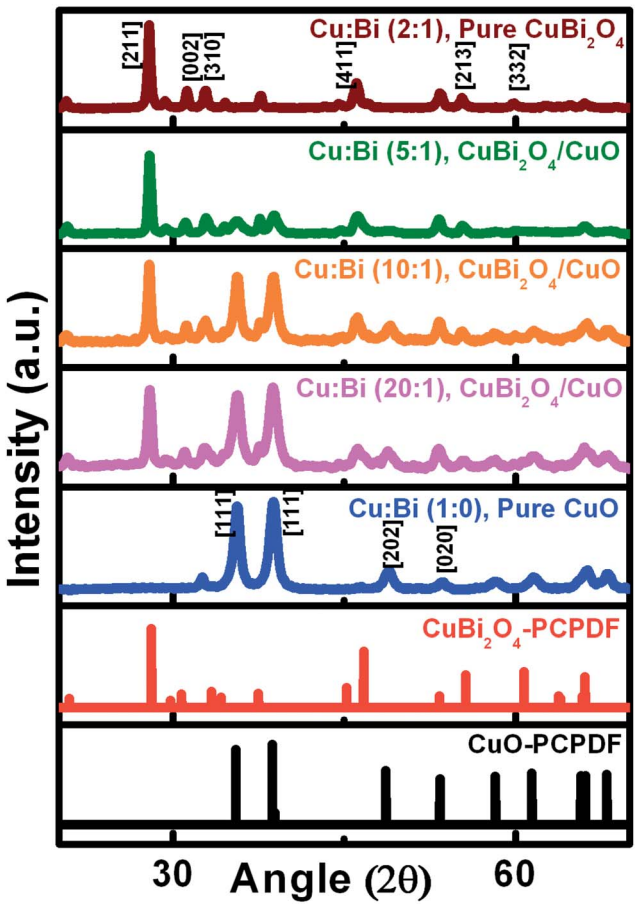

Fig. 7 X-ray diffraction data of pure phase $CuBi_2O_4$, CuO and all three nonstoichiometric cases indicating the presence of $CuBi_2O_4$, and CuO in the nanocomposite.

Amongst the nonstoichiometric $CuBi_2O_4$ cases, for the 10 : 1 ratio of Cu : Bi, the spherulitic morphology is completely dismantled into nanorods and nanosheets. Therefore, as with the earlier morphology evolution study with time for pure $CuBi_2O_4$, this non-stoichiometric case was also studied at reaction times of 0 min, 30 min, 60 min and 120 min. The morphology images at corresponding instances are presented in Fig. 8.

At 0 min, there are aggregated particles looking similar to what we observed for the pure $CuBi_2O_4$ case. After half an hour of reaction time the particles start interconnecting with each other to form small rods and spindles of rods. These structures grow further and at the end of two hours we observe a mixture of rods and some undefined anisotropic structures. The TEM images shown in Fig. 5(A) and (B) more clearly reveal the nature of these structures.

It is now useful to make a few remarks on the connection between non-stoichiometry and phase/morphology evolution. The formation of spherulitic flowers can be attributed to the peculiar characteristics of hydrogen bonding in the ethanol–water mixture[23] and the pH of the solution. When ethanol and

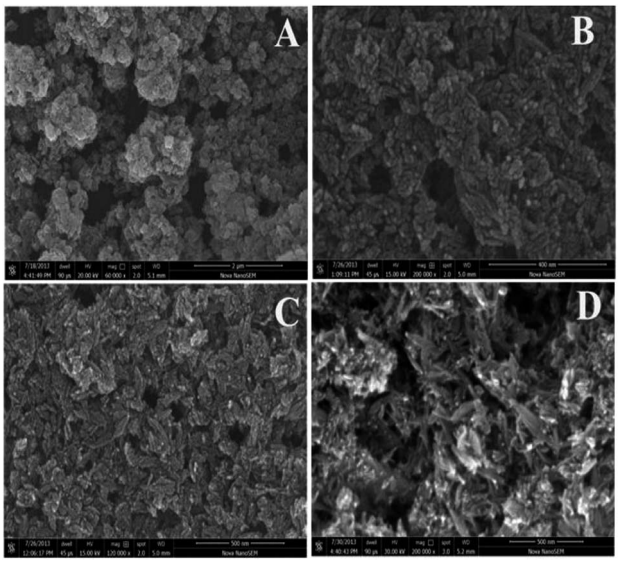

Fig. 8 SEM images of the $CuBi_2O_4$–CuO composite obtained at 0 min (A), 30 min (B), 60 min (C) and 120 min (D) respectively.

water are mixed together, the water molecules bind preferentially to the alcohol molecules and the resultant dielectric constant of the mixture decreases, facilitating stronger electrostatic interaction between the charged segments in the molecules.

In such cases hydrophobic interactions play an important role in different surface-interface processes such as self-assembly of molecules on surfaces and the aggregation behaviour of micelles. Initially tiny nanoparticles of $CuBi_2O_4$ can get nucleated and these can get attached to each other progressively forming self-assembled spherulites. Since in this case all the growing nuclei belong to the same crystal system, there are several options for oriented attachments[24–26] along all directions with favourable crystal planes leading to 3D-type morphology. This can be viewed as 3D random sequential adsorption with some restrictions related to the relative crystallographic orientations of the attaching grains. The alkaline pH of solution can assist in the growth of micron-sized spherulites under such conditions. The presence of the OH^- ion can influence the agglomeration process to give large shape. This is the way for nanoparticles to self-assemble by sharing their common crystallographic orientation at planar interfaces.

As shown, under non-stoichiometric growth with excess copper precursor, a mixed phase of $CuBi_2O_4$ and CuO is obtained, and these two compounds belong to two different crystal forms, namely tetragonal and monoclinic, respectively. Since the lattice plane compatibility conditions are highly limited in such a case, the oriented attachments are expected to have a high degree of orientation selectivity, conducive to anisotropic morphologies such as nanorods or nanosheets, as observed. In addition to the inter-phase attachments, the crystal habits of the two separate systems will be additional drivers, which can then define the separate phase morphologies in the overall microstructure.

Besides morphology, the most prominent change brought about by the non-stoichiometric synthesis leading to the $CuBi_2O_4$–CuO composite is the increase in the surface area. The Brunauer–Emmett–Teller (BET) surface area of pure spherulitic $CuBi_2O_4$ is around 6 $m^2\ g^{-1}$, which increases by more than 9 times, to 55 $m^2\ g^{-1}$ for the case of the $CuBi_2O_4$–CuO composite. This aspect is extremely important in the context of photoelectrochemical applications, especially for water splitting since higher interface area with water provides a more intimate contact of nanoparticles with the electrolytes and the photogenerated minority charge carriers have to travel lesser distance for water reduction–oxidation. For materials with poorer electronic properties such as $CuBi_2O_4$, this improvement is even more significant. Hence we investigated the performance of these two systems for photoelectrochemical water splitting application as discussed in the next section.

The optical properties of $CuBi_2O_4$, $CuBi_2O_4$–CuO composite and CuO (for reference) measured by diffused reflectance spectra in the range from 200 nm to 1800 nm are presented in Fig. 9. The band gap values for pure $CuBi_2O_4$ and pure CuO as obtained from Tauc's plots are 1.74 eV and 1.35 eV, respectively, as shown in the inset. The $CuBi_2O_4$–CuO composite shows tailing in the infrared region which could be due to some charge transfer states between $CuBi_2O_4$ and CuO because of their overlapping band alignment.

Fig. 10 presents the photoelectrochemical water splitting performance for spherulitic $CuBi_2O_4$, non-stoichiometrically prepared (10 : 1) $CuBi_2O_4$–CuO nanocomposite and pure CuO (as control). The performance data for the other non-stoichiometrically prepared samples with Cu : Bi ratios of 5 : 1 and 15 : 1 are presented in ESI-III.†

The *J*–*V* plot presented in Fig. 10 was recorded under a three electrode set-up with 0.1 M Na_2SO_4 as an electrolyte and under chopping light (that is alternatingly light on and off conditions). Now first it can be observed that $CuBi_2O_4$, CuO as well as the composite, all show a photoresponse at negative applied potentials with respect to the Ag/AgCl reference electrode and show a negative photocurrent. This suggests that they act as a

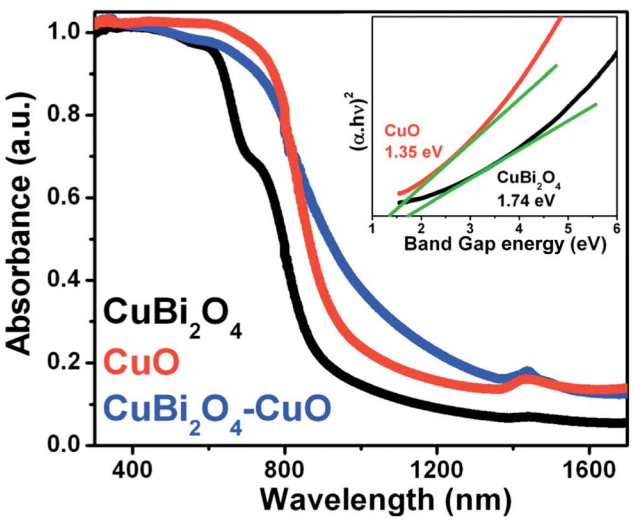

Fig. 9 UV-visible DRS spectra of pure $CuBi_2O_4$, CuO and the $CuBi_2O_4$–CuO composite.

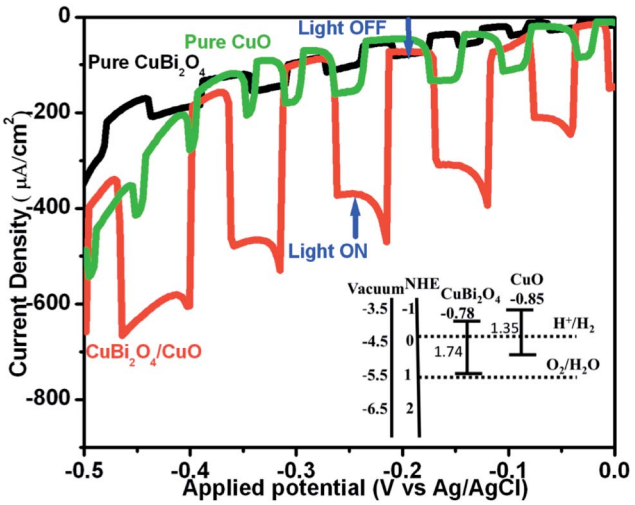

Fig. 10 Photoelectrochemical performances of $CuBi_2O_4$, CuO and the nonstoichiometric $CuBi_2O_4$–CuO composite in a 0.1 M sodium sulphate electrolyte under chopped irradiation of light. The inset shows the relative band alignment of $CuBi_2O_4$ and CuO.

photocathode in this photoelectrochemical system. Only a p-type semiconductor photocatalyst, under the applied potentials negative to their flatband potentials, can have a depletion region near the interface and hence can show any response to the incident light. Hence like CuO, pure $CuBi_2O_4$ is also showing p-type, photocathodic behaviour. The photocurrent performances are analyzed and compared at −0.4 V *vs.* Ag/AgCl. Beyond −0.5 V *vs.* Ag/AgCl the dark current starts to rise substantially. The maximum photocurrent density at −0.4 V for pure spherulitic $CuBi_2O_4$ is found to be ~40 μA cm^{-2}, while that for pure CuO is ~150 μA cm^{-2}. Most interestingly the non-stoichiometrically synthesized heterostructure composite of $CuBi_2O_4$–CuO shows an almost 10 times higher photocurrent density (~400 μA cm^{-2}) as compared to pure $CuBi_2O_4$. A major contribution to this performance enhancement certainly emanates from the enhanced surface area as mentioned earlier.

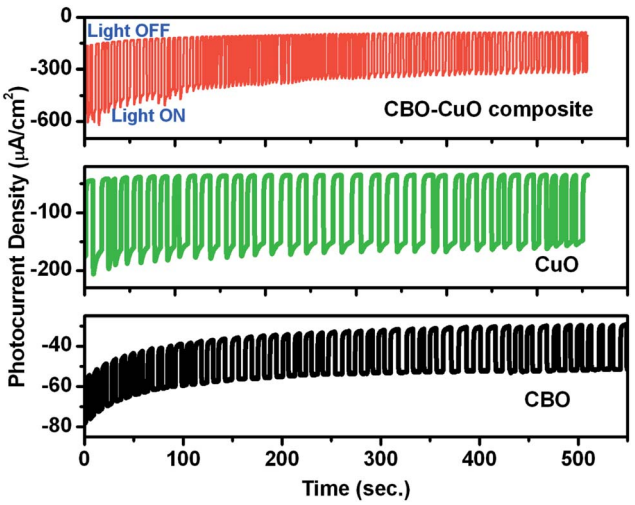

Fig. 11 Stability study of $CuBi_2O_4$, CuO and the $CuBi_2O_4$–CuO composite at −0.4 V *vs.* Ag/AgCl.

We note however that the CuO nanostructure with comparable area and similar morphology alone does not give equivalent or comparable performance. This implies that another factor is also in play which is the charge separation at the $CuBi_2O_4$–CuO interface.

The relative conduction and valence band positions of $CuBi_2O_4$ and CuO obtained from cyclic voltammetry are shown in the inset of Fig. 10. The cyclic voltammetry data are presented in ESI-IV.† The observed band positions are consistent with the literature.[14,16,27] This suggests that $CuBi_2O_4$ and CuO have a type-II relative band alignment, which facilitates the photogenerated charge separation at their interface and reduces charge recombination. Thus the nano-heterostructure of $CuBi_2O_4$–CuO shows a strong influence of both the enhanced surface area and suppressed charge recombination on its water-splitting performance.

Since the stability of copper based photocathodic materials is a major issue of concern, we measured the current *vs.* time data of pure and nanocomposite samples at the applied potentials of −0.4 V *vs.* Ag/AgCl for 10 minutes as shown in Fig. 11. Above −0.4 V *vs.* Ag/AgCl Cu^{2+} reduces to Cu^{+} and further to Cu,[28] hence the system does not remain stable. The photocurrent density of the composite seems to decrease to ~65% after 10 minutes. In comparison with Cu_2O, which is considered as the most efficient but unstable (PEC performance drops down quickly in minutes) copper based photocathodic material so far,[27] the stability of our nanocomposite is much better. Moreover, other strategies such as atomic layer deposition (ALD) of suitably chosen metal oxides could be envisioned and implemented to offer further protection to the nanocomposite system.

Conclusion

In this work, we report low temperature crystal growth of copper bismuth oxide with a rich morphology. By controlling the type of solvent, temperature, and time, we could tune the morphology of $CuBi_2O_4$ to highly porous interconnected structures, porous spheres and spherulites. Furthermore, with non-stoichiometric addition of excess copper we could engineer a nano-heterostructure composite of $CuBi_2O_4$ and CuO, where $CuBi_2O_4$ formed nanorods and CuO formed nanosheets. This transformation concurrently yielded a high surface area and, due to favourable charge separation kinetics, demonstrated remarkable enhancement in the photoelectrochemical water splitting performance.

Acknowledgements

The authors gratefully acknowledge the Department of Science and Technology (Nanomission), Govt of India, and TAPSUN program of CSIR for funding. We also thank Mr Mangesh Kokate for help in BET measurement.

References

1 M. J. Bierman and S. Jin, *Energy Environ. Sci.*, 2009, **2**, 1050–1059.

2 Y. Wei, L. Ke, J. Kong, H. Liu, Z. Jiao, X. Lu, H. Du and X. W. Sun, *Nanotechnology*, 2012, **23**, 235401–235409.

3 J. Su, X. F. Jennifer, D. Sloppy, L. Guo and C. A. Grimes, *Nano Lett.*, 2011, **11**, 203–208.

4 Z. Zhang and P. Wang, *Energy Environ. Sci.*, 2012, **5**, 6506–6512.

5 Y. J. Hwang, C. H. Wu, C. Hahn, H. E. Jeong and P. Yang, *Nano Lett.*, 2012, **12**, 1678–1682.

6 H. Kim, M. Seol, J. Lee and K. Yong, *J. Phys. Chem. C*, 2011, **115**, 25429–25436.

7 J. Liu, H. Wang, S. Wang and H. Yan, *J. Mater. Sci. Eng. B*, 2003, **104**, 36–39.

8 Z. Jiao, J. Wang, L. Ke, X. W. Sun and H. V. Demir, *ACS Appl. Mater. Interface*, 2011, **3**, 229–236.

9 G. Wang, H. Wang, Y. Ling, Y. Tang, X. Yang, R. C. Fitzmorris, C. C. Wang, J. Z. Zhang and Y. Li, *Nano Lett.*, 2011, **11**, 3026–3033.

10 S. Shet, K. S. Ahnc, T. Deutscha, H. Wanga, R. N. Y. Yana, J. Turnera and M. Al-Jassima, *J. Power Sources*, 2010, **195**, 5801–5805.

11 Z. Zhang and P. Wang, *J. Mater. Chem.*, 2012, **22**, 2456–2464.

12 S. Kelkar, P. Shaikh, P. Pachfule and S. Ogale, *Energy Environ. Sci.*, 2012, **5**, 5681–5685.

13 S. Kelkar, C. Ballal, A. Deshpande and S. Ogale, *J. Mater. Chem. A*, 2013, **1**, 12426–12431.

14 T. Arai, M. Yanagida, Y. Konishi, Y. Iwasaki, H. Sugihara and K. Sayama, *J. Phys. Chem. C*, 2007, **111**, 7574–7577.

15 T. Arai, Y. Konishi, Y. Iwasaki, H. Sugihara and K. Sayama, *J. Comb. Chem.*, 2007, **9**, 574–581.

16 W. Liu, S. Chen, S. Zhang, W. Zhao, H. Zhang and X. Yu, *J. Nanopart. Res.*, 2010, **12**, 1355–1366.

17 N. T. Hahn, V. C. Holmberg, B. A. Korgel and C. B. Mullins, *J. Phys. Chem. C*, 2012, **116**, 6459–6466.

18 A. M. Abdulkarem, J. Li, A. A. Aref, L. Ren, E. M. Elssfah, H. Wang, Y. Ge and Y. Yu, *Mater. Res. Bull.*, 2011, **46**, 1443–1450.

19 S. Das, S. Kar and S. Chaudhuri, *J. Appl. Phys.*, 2006, **99**, 114303–114310.

20 J. K. Bailey, C. J. Brinker and M. L. Mecartney, *J. Colloid Interface Sci.*, 1993, **157**, 1–13.

21 V. Privman, D. V. Goia, J. Park and E. Matijevic, *J. Colloid Interface Sci.*, 1999, **213**, 36–45.

22 R. L. Penn and J. F. Banfield, *Science*, 1998, **281**, 969–971.

23 S. N. Yu, L. Guillaume and R. Benoit, *J. Phys. Chem. B*, 2005, **109**, 6705–6713.

24 C. Viedma, J. M. Mc Bride, B. Kahr and P. Cintas, *Angew. Chem., Int. Ed.*, 2013, **52**, 10545–10548.

25 Y. W. Jun, J. S. Choi and J. Cheon, *Angew. Chem., Int. Ed.*, 2006, **45**, 3414–3439.

26 J. S. Chen, T. Zhu, C. M. Li and X. W. Lou, *Angew. Chem., Int. Ed.*, 2011, **50**, 650–653.

27 Q. Huang, F. Kang, H. Liu, Q. Li and X. Xiao, *J. Mater. Chem. A*, 2013, **1**, 2418–2425.

28 D. Grujicic and B. Pesic, *Electrochim. Acta*, 2005, **50**, 4426–4443.